CHEMISTRY OF MATERIALS

pubs.acs.org/cm

Article

Nonclassical Crystallization Pathway of Transition Metal Phosphate Compounds

Stephanos Karafiludis,* Zdravko Kochovski, Ernesto Scoppola, Anika Retzmann, Vasile-Dan Hodoroaba, Johan E. ten Elshof, Franziska Emmerling, and Tomasz M. Stawski*

Cite This: *Chem. Mater.* 2023, 35, 10645−10657

Read Online

ACCESS | Metrics & More | Article Recommendations | Supporting Information

ABSTRACT: Here, we elucidate nonclassical multistep crystallization pathways of transition metal phosphates from aqueous solutions. We followed precipitation processes of M-struvites, $NH_4MPO_4{\cdot}6H_2O$, and M-phosphate octahydrates, $M_3(PO_4)_2{\cdot}8H_2O$, where M = Ni, Co, or Ni_xCo_{1-x}, by using *in situ* scattering and spectroscopy-based techniques, supported by elemental mass spectrometry analyses and advanced electron microscopy. Ni and Co phosphates crystallize *via* intermediate colloidal amorphous nanophases, which change their complex structures while agglomerating, condensing, and densifying throughout the extended reaction times. We reconstructed the three-dimensional morphology of these precursors by employing cryo-electron tomography (cryo-ET). We found that the complex interplay between metastable amorphous colloids and protocrystalline units determines the reaction pathways. Ultimately, the same crystalline structure, such as struvite, is formed. However, the multistep process stages vary in complexity and can last from a few minutes to several hours depending on the selected transition metal(s), their concentration, and the Ni/Co ratio.

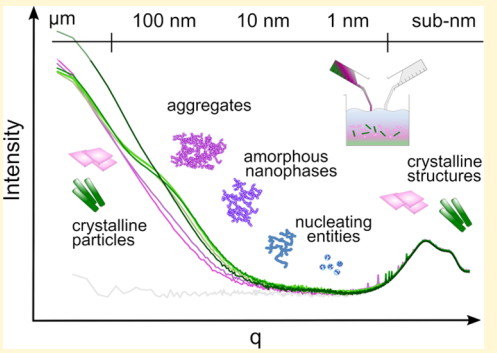

INTRODUCTION

A key factor in ensuring the sustainable use of raw materials to meet global demand has been the recovery and reuse of key components. Phosphate, PO_4^{3-}, and many transition metals are listed as critical raw materials.[1−3] Moreover, these elements may cause adverse effects on the environment. Phosphorus is the major culprit in anthropogenic eutrophication. Transition metal ions are toxic pollutants, especially in groundwater and wastewater. Therefore, coprecipitation of phosphate and transition metal-bearing phases from various waste streams of agricultural, industrial, or mining origin (tailings, sludge, wastewaters) is a viable extraction and recycling method to yield transition metal phosphates (TMPs).[4,5] Such materials could be further upcycled into processed, higher value compounds suitable for applications. For example, transition metal phosphates, such as Zr,[6] Sn,[7] Ni, or Co[8] phosphates, garnered attention as low-cost, chemically stable, and tunable proton conductors for fuel cells.[9−16] However, to effectively harvest metal and phosphate in the form of TMPs and convert them to functional materials, one must elucidate their nucleation and crystallization pathways from aqueous solutions. Although the synthesis and precipitation of Mg or Ca phosphate-bearing phases are relatively well-characterized,[17−19] investigations of the crystallization of transition metal phosphate materials are scarce and focus on mineralogical aspects.[20] Most of the available studies concentrate on the incorporation or adsorption of transition metals and metalloids[10,21−24] rather than their complete substitution in phosphate-based compounds.[25−27] However, TMPs exhibit major differences in their crystallization pathways, growth kinetics, thermodynamic stabilities, or transformations among each other and differ from their related main-group analogues.[28,29]

The traditional view of crystallization and nucleation through a classical model has been widely used to describe chemical systems since its establishment in the 19th century.[30,31] This is mainly because of its simplicity and the ability to make accurate predictions. The classical crystallization theory (CCT) assumes a layer-by-layer growth of primary crystal nuclei due to the adsorption of growth units/monomers (atoms, ions, molecules) on the crystal surface/kinks and their following reconfiguration to a new interface. Although CCT works well for model systems,[32,33] a frequent number of complex interactions could not be explained by this theory due to its simplified assumptions and limitations, *i.e.*, capillary assumption or considering only single particle attachment. Theoretical predictions tend to deviate significantly from experimental results in orders of magnitude in nucleation and reaction rates of the crystalline

Received: September 13, 2023
Revised: November 20, 2023
Accepted: November 21, 2023
Published: December 12, 2023

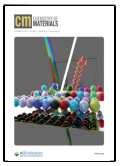

Table 1. Summary of the Methods Used and the Associated Research Goals According to Their Importance[a]

method	description	*ex/in situ*	solute/solid/both	research goal
SAXS/WAXS	time-resolved X-ray scattering and diffraction	*in situ*	both	time-resolved particle sizes of hierarchical structures, reaction kinetics, and mechanism
cryo-TEM	imaging and 3D reconstruction	*ex situ*	solid	imaging morphology, size, and structure of amorphous phase
	electron diffraction	*ex situ*	solid	determination of crystal structure
ICP-MS	dissolved solids	*ex situ*	solid	elemental information about the solids
	particle-filtered mother solution	*ex situ*	solute	elemental information about the solutes
SEM	imaging	*ex situ*	solid	imaging morphology, size, and structure of final crystalline phases
EDX	mapping and line scans	*ex situ*	solid	elemental information about the solids
XRD	powder, Bragg−Brentano	*ex situ*	solid	phase composition
pH	time-resolved pH measurements	*in situ*	both	reaction kinetics and mechanism
CTEM	imaging	*ex situ*	solid	imaging morphology, size, and structure of amorphous phases
EDX	mapping	*ex situ*	solid	elemental information about the solids
FT-IR	attenuation	*ex situ*	solid	elemental information and phase composition of the solids

[a]The crystallization process was analyzed by a combination of imaging-, spectroscopic-, spectrometric-, and scattering-based *ex situ* and *in situ* methods.

particles.[34−38] Different experimental studies and approaches demonstrated empirically multiple possible formation pathways toward the final crystal through the inclusion of prenucleation clusters,[39] liquid droplets, gels, primary amorphous or crystalline nanoparticles, nanoaggregates,[4] or mesocrystals.[40] In the past two decades, a large variety of these transitional precursor phases of crystalline substances were discovered in pharmaceuticals,[41,42] proteins,[43−45] organic molecules,[46,47] thin films,[48,49] biominerals,[39,50] and inorganic materials.[4,46,51−53]

As we demonstrate in this work, TMPs follow a nonclassical crystallization pathway, which includes evolving amorphous precursors before the final formation of a crystal. We holistically elucidate the crystallization behavior of transition metal phosphate phases, from their intermediate amorphous nanophases in solution, through aggregates and protocrystalline units, to final crystals. The formation processes are analyzed in detail with various diffraction- and spectroscopy-based ex- and *in situ* approaches. Ni and Co ions can both be incorporated into the same crystalline structures (*i.e.*, struvite or octahydrate). However, the crystallization stages of these analogous TMPs are essentially different.[4,54] We also demonstrate that in a dual Ni_xCo_{1-x} metal mixtures, compared to the pure cases, an even more complex pathway is induced. Here, the Ni/Co ratio and the concentration of both metals have a major influence on the reaction kinetics and the crystallization outcome. In this work, we provide insights into how two 3d metal ions, Ni and Co, interact with each other, resulting in changes in reaction time and crystallization stages of the phosphate precipitation.

METHODS

Synthesis. $(NH_4)_2HPO_4$ (DAP) (ChemSolute, 99%), $NiSO_4 \cdot 6H_2O$ (ChemSolute, 99%), and $CoSO_4 \cdot 7H_2O$ (Alfa Aesar, 98%) were used to synthesize M-phosphates (M = Ni, Co, Ni_xCo_{1-x}). At first, 1 mol/L stock solutions of DAP and the metal salts were prepared. The detailed synthesis procedure can be found elsewhere.[4] The transition metal and DAP concentrations in the aqueous solution were varied from 0.004 to 1 mol/L, resulting in a metal-to-phosphate ratio $0.2 \leq MP \leq 1$. By using DAP with a fixed nitrogen-to-phosphate ratio of 2, the precipitation reaction of M-struvite typically occurred according to the following mass-balance equation

$$6H_2O + NH_4^+{}_{(aq)} + H_xPO_4^{3-x}{}_{(aq)} + M^{2+}{}_{(aq)} \rightarrow NH_4MPO_4 \cdot 6H_2O_{(s)} + xH^+{}_{(aq)} \quad (1)$$

Equation 1 was, in general, valid for Ni, regardless of the metal concentration used and for Co at lower concentrations below an MP ratio of 0.4.[54] However, at high concentrations of Co^{2+}, above an MP ratio of 0.4, we observed the crystallization of cobalt(II)phosphate octahydrate (CPO) instead of Co-struvite (COS) according to eq 2

$$8H_2O + 2H_xPO_4^{3-x}{}_{(aq)} + 3Co^{2+}{}_{(aq)} \rightarrow Co_3(PO_4)_2 \cdot 8H_2O_{(s)} + 2xH^+{}_{(aq)} \quad (2)$$

We also investigated (Ni_xCo_{1-x}) mixtures, for which we defined Ni numbers (Ni#). Following eq 3, we varied Ni# from 0.1 (Co-rich) to 0.95 (Ni-rich).

$$Ni\# = \frac{c(Ni^{2+})}{c(Ni^{2+}) + c(Co^{2+})} \quad (3)$$

For any analyses requiring dry crystalline powders, the solid phases precipitated in solutions were collected onto a cellulose filter (pore size of 1 μm, LABSOLUTE) by using a vacuum filtration kit (*i.e.*, Büchner funnel). Afterward, the powders were washed with distilled water and left to dry at room temperature in air for 2 h.

To elucidate the crystal formation pathways, we used various *in situ* and *ex situ* characterization methods (Table 1), with which we analyzed solids in solution, dry solids, and supernatants at different stages. Detailed technical descriptions of the used characterization methods, including X-ray diffraction (XRD) for identification of the phase composition, pH measurements to monitor the precipitation reaction, infrared spectroscopy (IR) for tracking the phosphate and water/ammonium environment in the solids, scanning electron microscopy (SEM) and conventional and cryogenic transmission electron microscopy (CTEM, cryo-TEM) for imaging, diffraction and elemental mappings/line scans and *in situ* small- and wide-angle X-ray scattering (SAXS/WAXS) for tracking amorphous phaser associated with the phase composition, and inductively coupled plasma mass spectrometry (ICP-MS) analysis for determining the changing chemical composition of liquid and solid as a function of time, can be found in the (Supporting Information (SI), Methods Section). The rationale behind the use of each method is described in Table 1.

RESULTS AND DISCUSSION

Overview of the Transitional Nanophases during Crystallization. The complexity of the crystallization pathways leading to a crystalline solid manifests itself through changes in the solid material, as well as in the complementary supernatant. Both pieces of this complementary "pair" need to be considered to fully understand the crystallization process. At the beginning of our investigations, we directly followed the reaction with usual laboratory methods, including XRD or pH. We used all those

https://doi.org/10.1021/acs.chemmater.3c02346
Chem. Mater. 2023, 35, 10645−10657

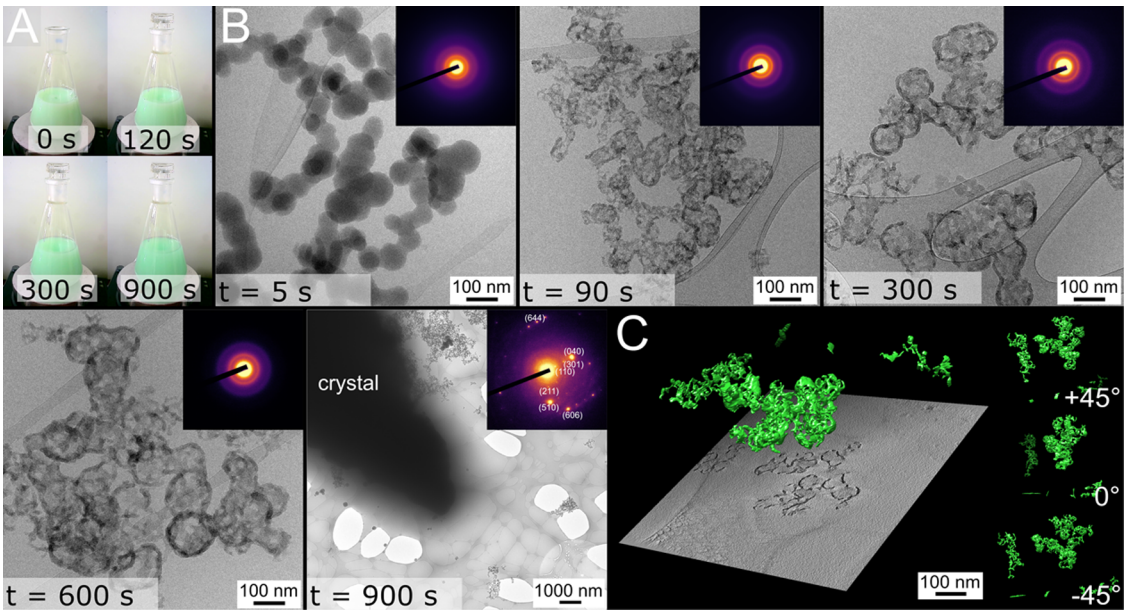

Figure 1. Cryo-TEM images and the tomographic reconstruction of Ni phosphates at different reaction steps/times (t = 5, 90, 300, 600, and 900 s) in the precipitation reaction. (A) Photographs of the temporal color changes in solution. (B) Detailed cryo-TEM image of the observed structures at a given reaction time, inset: associated SAED pattern with significant marked crystalline facets. (C) Three-dimensional volume rendering from a cryo-ET reconstruction shown over a central XY slice from the reconstruction at t = 300 s, insets in (C): The three-dimensional particle surface renderings at selected angles from −45° < 0° < +45°: a full movie of the reconstruction and additional images can be found in the SI, Figure S3. The measurements were supplemented with EDX maps in CTEM, with which we confirmed the presence of N, P, O, and M with M = Ni or Co in the observed aggregates but we also observed their decomposition by degassing of volatile compounds (SI, Figure S3).

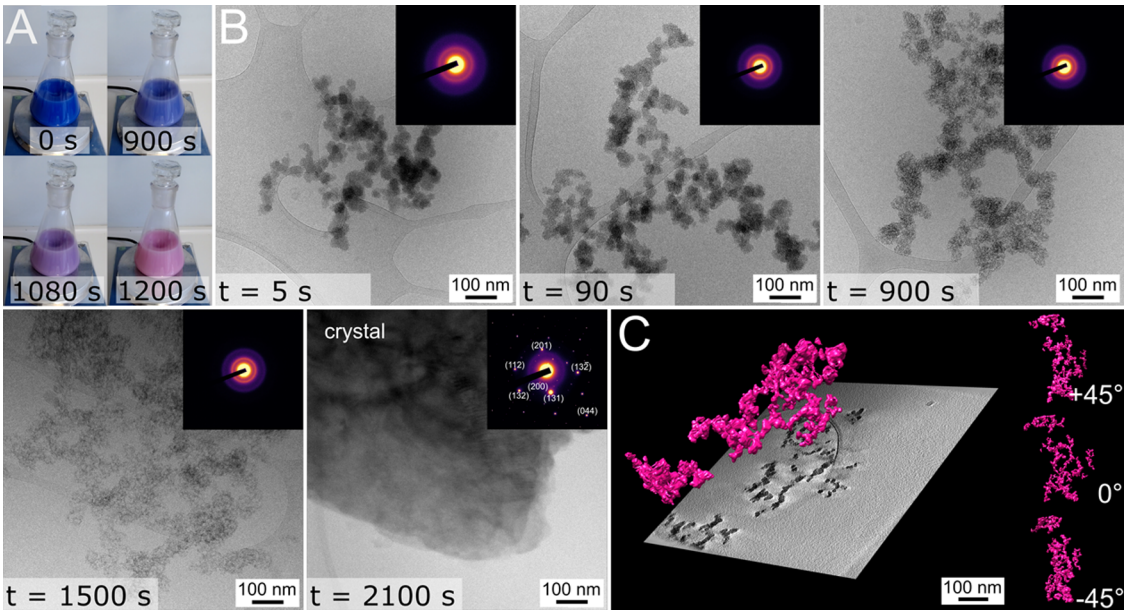

Figure 2. Cryo-TEM images and tomographic reconstruction of Co phosphates at different reaction steps/times (t = 5, 90, 900, 1500, and 2100 s) in the precipitation reaction. (A) Photographs of temporal color changes in solution; (B) detailed cryo-TEM image of the observed structures at a given reaction time, inset: associated SAED pattern with marked crystalline facets; (C) three-dimensional volume rendering from a cryo-ET reconstruction shown over a central XY slice from the reconstruction (t = 900 s), insets in (C): three-dimensional particle surface renderings at selected angles from −45° < 0° < +45°. Full movies of the tomographic reconstruction and additional images can be found in the SI.

observations to establish a baseline for advanced *in situ* methods and pinpoint characteristic moments for *ex situ* methods (Table 1). During the crystallization of TMPs, protons are released (eqs 1 and 2); therefore, time-resolved pH measurements provide partial insights into the formation process of these materials. Thus, from simple pH trends, we can identify the characteristic events in the crystallization pathway and indeed confirm the multistep nature of the mechanism. We further prove with various *in situ* and *ex situ* methods (Table 1) that the multistep evolution involves transitional amorphous nanophases preceding the formation of the final crystals.

Moreover, a directly observable color change of the aqueous solutions/slurries of TMPs also hints toward potential phase evolution and indicates the multistep character (*e.g.*, liquid−

https://doi.org/10.1021/acs.chemmater.3c02346
Chem. Mater. 2023, 35, 10645−10657

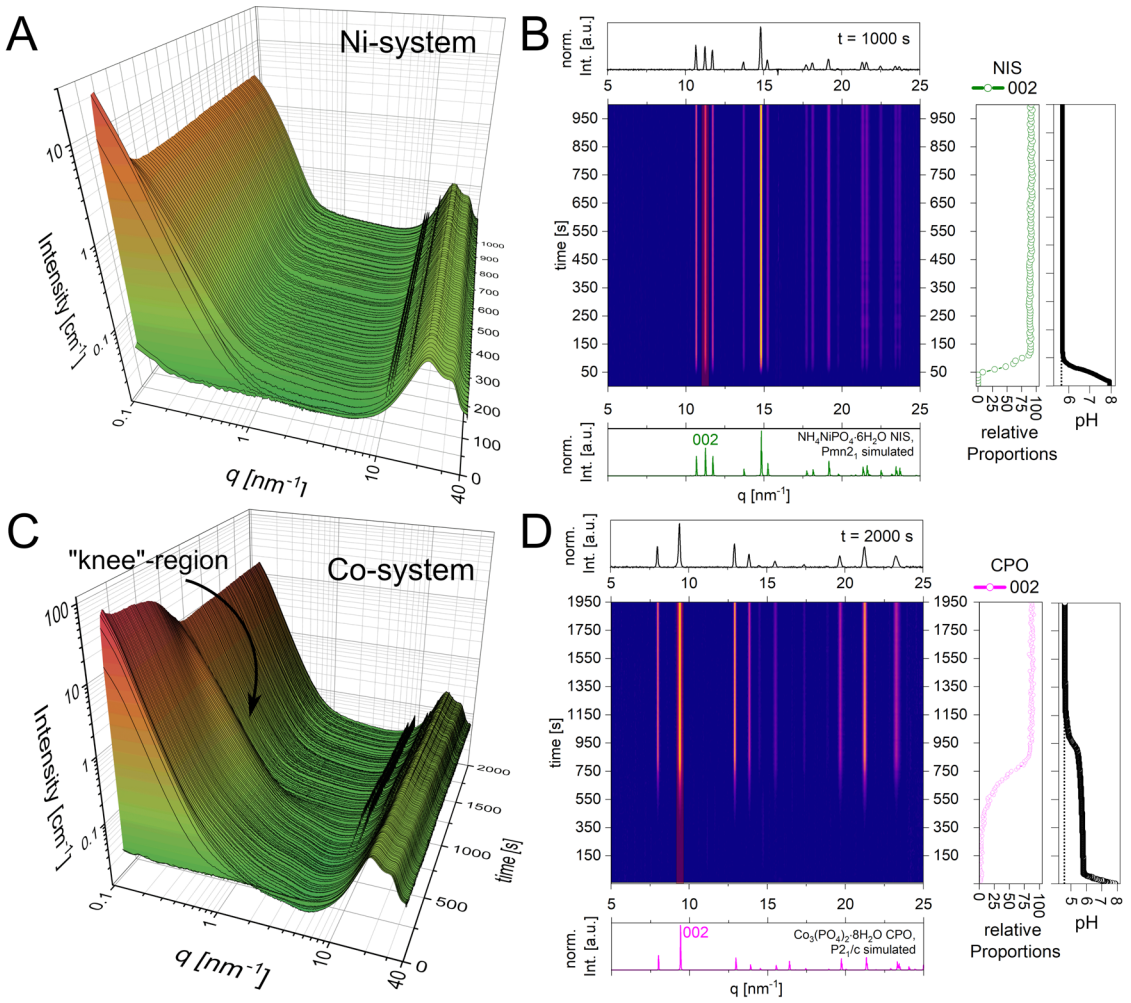

Figure 3. *In situ* SAXS/WAXS data from crystallization experiments measured with a flow-through setup (SI, Figure S6) of the pure Ni system and of the Co system. In panel (A), the entire scattering data are displayed in a three-dimensional surface diagram through time, while in panel (B), the WAXS data are summarized in heatmaps for the Ni system. In panel (C), the entire scattering data are displayed in a three-dimensional surface diagram through time, while in panel (D), the WAXS data are summarized in heatmaps for the Co system. The low-intensity SAXS curves at the beginning represent the premixed stage of the pure DAP solution before injection of the metal-bearing solution. WAXS heatmaps: normalized WAXS intensities plotted with simulated crystal structures and the final WAXS signal of the experiment. On the right side: normalized intensity of a characteristic (002) reflection of the crystalline phase and simultaneously measured *in situ* pH data with the final equilibrated pH of the experiment marked by the dotted line (NIS = Ni-struvite, CPO = Co-phosphate octahydrate) marked with a red frame. Ni-struvite reference ICSD 403058, Co-phosphate octahydrate reference 2020362. SAXS data: Projection of time-resolved normalized SAXS data with colored intensities.

amorphous, liquid−crystalline, and amorphous−crystalline transformations). As we demonstrated in a previous work, the color change directly indicates an extensive change in the transition metal coordination environment associated with the transformation of the solids, *e.g.*, from an amorphous to a crystalline state This involves further structural ordering and reorganization.[4] Even by observing the evolving solutions, one can determine characteristic moments in time, where the nature of solids changes, pointing out to a nonclassical nature of the crystallization processes.

Accordingly, as indicated by the found pH trends (SI, Figure S2) and the color changes, for investigations of the intermediate amorphous nanophases, cryo-TEM measurements were performed at selected reaction times for the pure Ni system (Figure 1) and the pure Co system (Figure 2). Importantly, Ni and Co exhibit clearly different reaction kinetics, where Ni fully develops within several minutes, while Co evolves over tens of minutes (≈10× factor difference). By the observation of the color change (Figures 1A and 2A) and the pH trends (SI, Figure S2), moments of interest in the crystallization pathway were selected and quenched using the cryo-TEM approach. Ideally, the interesting stages should comprise the formation of the smallest to largest nucleating entities until their final transformation into a crystal.

Indeed, we observed complex amorphous particulate morphologies before any crystals were formed. For both Ni-PO_4 (Figure 1B) and Co-PO_4 (Figure 2B), the as-observed intermediate solids are amorphous, as indicated by selected area electron diffraction (SAED) (see the insets in each micrograph). Interestingly, the precursors have a three-dimensional (3D) morphology evidenced by the electron density contrast and branched agglomeration topology. Thus, even after the immediate pH drop due to mixing phosphate and metal solutions (SI, Figure S2) associated with color change (Figure 1B), the initial moments of crystallization do not yield crystalline but amorphous solids. We visualized these 3D structural features in the complex amorphous framework of the nanophases by performing cryo-electron tomography (cryo-ET).[55] In Figures

https://doi.org/10.1021/acs.chemmater.3c02346
Chem. Mater. 2023, 35, 10645−10657

1C and 2C, a gallery of XY slices of the amorphous Ni- and Co-phosphate nanophases at t = 5 min (Ni) and t = 10 min (Co) are presented. Using segmentation and subsequent surface rendering of the particles in the tomographic reconstruction, the three-dimensional internal structure of the compounds can be revealed. At the early stages (t = 5 s) of the reaction, the Ni system forms regular spherical amorphous nanoparticles of around 50 nm diameter agglomerated to micrometer-sized large frameworks (Figure 1B,C). With progressive reaction times (t = 90, 300, and 900 s), the extent of agglomeration increases while particles also develop dense outer shells and hollow interiors (Figure 1C). From cryo-ET imaging, the observed structure comprises interconnected tubes with dense shells and a voluminous interior. After t = 300 s, the agglomerates coalesce to a final micrometer-sized crystal of Ni-struvite at t = 900 s. These single crystals show a regular faceted morphology and exhibit the usual diffraction spots in the SAED pattern. The actual transformation of the amorphous Ni phases to a final crystal can also be correlated with the pH trends, where the pH equilibrates within 5 min, regardless of the nickel concentration (SI, Figure S2A−D).

In the Co system (Figure 2), the observed trends are similar to those for Ni. First (Figure 2B, t = 5−900 s), near-spherical particles agglomerate into larger units, and all the involved species are amorphous until 1500 s (see SAED in Figure 2B). Noticeably, the particles at 5 s are highly irregular and smaller than those in the Ni system (average size of Ni: 50 nm compared to the average size of Co: 35 nm). Again, these agglomerating frameworks progressively condense with increasing reaction times and form larger assemblies of up to 1500 s. After t = 2100 s, final micrometer-sized single crystals appeared, showing a highly regular faceted structure with clear diffraction spots in the SAED pattern. Videos of the tomographic reconstruction of the Ni- and Co-PO_4 precursors based on the cryo-TEM micrographs in different orientations are attached in the SI. Based on the pH curves and the cryo-TEM monitoring, the Co system demonstrates a significantly longer time (∼10× factor) to reach reaction equilibrium compared to the pure Ni system, which is, in addition, dependent on the initial Co concentration in solution. Looking at the pH measurements of the Co system, the time to reach an equilibrium pH and its value itself change starkly after increasing the metal concentration above 0.04 mol/L (MP > 0.4) [t = 500 s for $c(Co^{2+})$ = 0.02 mol/L, MP = 0.2, pH_{eq} = 5.6 to t = 3500 s for $c(Co^{2+})$ = 0.04 mol/L, MP = 0.4, pH_{eq} = 4.5]. Here, the kinetics and the decrease in pH behavior can be explained by a change in the final crystalline product. Specifically, with increasing Co concentration, the crystallization pathway leads to either Co-struvite ($c(Co^{2+})$ < 0.04 mol/L, MP = 0.4, eq 1) or Co-phosphate octahydrate ($c(Co^{2+})$ > 0.04 mol/L, MP = 0.4, eq 2).[4] Consequently, the increasing Co^{2+} concentration induces a shift toward lower values in the pH curves at around MP ≈ 0.4 (SI, Figures S1−S3).[4,28,54] Since the Ni system always leads to Ni-struvite, regardless of the metal concentration, the pH trends for this system exhibit practically constant final values (SI, Figure S1). Based on the multistep patterns observed in the pH curves and the transformation of the three-dimensional framework of the intermediate phases, we assume a complex interplay among amorphous and crystalline solids and possibly smaller species in solution in the form of (aqueous) clusters.

Time-Resolved Crystallization of the Pure Systems: From Ions to Amorphous Phases to a Final Crystalline Facet. From the results, including time-resolved pH measurements, visual observations, and cryo-TEM imaging, we correlated information about the morphology and structure of the transitional nanophases with the specific moments in time. However, such an *ex situ* quenching approach is limited by the realistically achievable time resolution and the number of samples that can be analyzed by electron microscopy. To gain more insights into the as-observed crystallization pathways, we wanted to simultaneously correlate the *in situ* morphological information with the temporal phase composition and reaction kinetics. This was achieved by using *in situ* approaches, avoiding any potential artifacts *e.g.*, from quenching. Therefore, *in situ* scattering (combined SAXS and WAXS) and pH measurements were performed to follow crystallization (see SI, Methods Section: *In situ* SAXS/WAXS). In this way, global information about the occurrence of crystalline phases and the presence and size of agglomerates with their building units could be quantified. As the hydrodynamic conditions between the cryo-TEM approach and the *in situ* SAXS/WAXS measurements exhibit significant differences, the time scales of crystallization deviate from one another.

Based on the occurrence of diffraction reflections in the pure Ni system (Figure 3A,B), Ni-struvite precipitates rapidly for t < 100 s as the sole crystalline phase. In the low-q region, at t < 100 s, after the injection of the metal-bearing solution, the scattering signal is dominated by a high-intensity scattering pattern, which implies the presence of large particles of the Ni-struvite crystals, manifesting themselves merely as a q^{-4} intensity dependence[56] (Porod interface). In contrast, Co-phosphate octahydrate precipitated much slower at t > 600 s, while the characteristic signal from the primary building units and their agglomerates was visible in the SAXS for q < 1 nm^{-1} (Figure 3B,C). Here, a so-called "knee" region can be identified with its centroid at around 0.4 nm^{-1}, indicating potentially polydisperse form factors of nucleating entities with different sizes (marked with an arrow in Figure 3). The precipitation of the actual crystals was completed only at t > 1500 s, evidenced by reaching an equilibrium pH of 4.7, the reduction of scattering intensity between 0.3−5 nm^{-1}, and the development of a Porod interface.

For quantitative analysis and the extraction of the microstructural descriptors, the SAXS part of the scattering data (*i.e.*, for 0.1 nm^{-1} < q < 3 nm^{-1}) was fitted with a unified model by Beaucage[57,58] (SI, Supporting Note 2, eq S3). A complete description of the model can be found in the SI (SI, Supporting Note 2, Figures S7−S10). From the SAXS fits, significant parameters are used for a system that assumes two distinct structural levels (smaller level denoted as sub), and therefore, we obtained B, G, G_{sub}, B_{sub}, R_g, and R_{sub} as a function of time (SI, Figure S7). In a nutshell, B and G values are Porod and Guinier prefactors, accordingly, while R values are radii of gyration. These variables parametrize the scattering profile throughout the considered q region. While R_g and R_{sub} are effectively limited by the measured q-range, the other parameters exhibit approximately different ranges, *e.g.*, $G \approx n100$ cm^{-1}, $G > G_{sub} > n10^{-6}$ cm^{-1} (where n i the multiple of), B and B_{sub} are mostly below 1. The p and p_{sub} parameters show values between 4 and 2, dependent on the interface of the scatterers (p = 4 for sharp, smooth Porod interfaces).

For the Ni system (SI, Figure S8), the evolution of the fitting parameters reflects a quick formation of micometer-sized large particles preceded by a fast conversion of the short-lived amorphous phases t < 100 s (SI, Figure S8). Here, the crystallization of Ni-struvite manifested itself in increasing G and G_{sub} values originating from the slope increase of the SAXS

https://doi.org/10.1021/acs.chemmater.3c02346
Chem. Mater. 2023, 35, 10645−10657

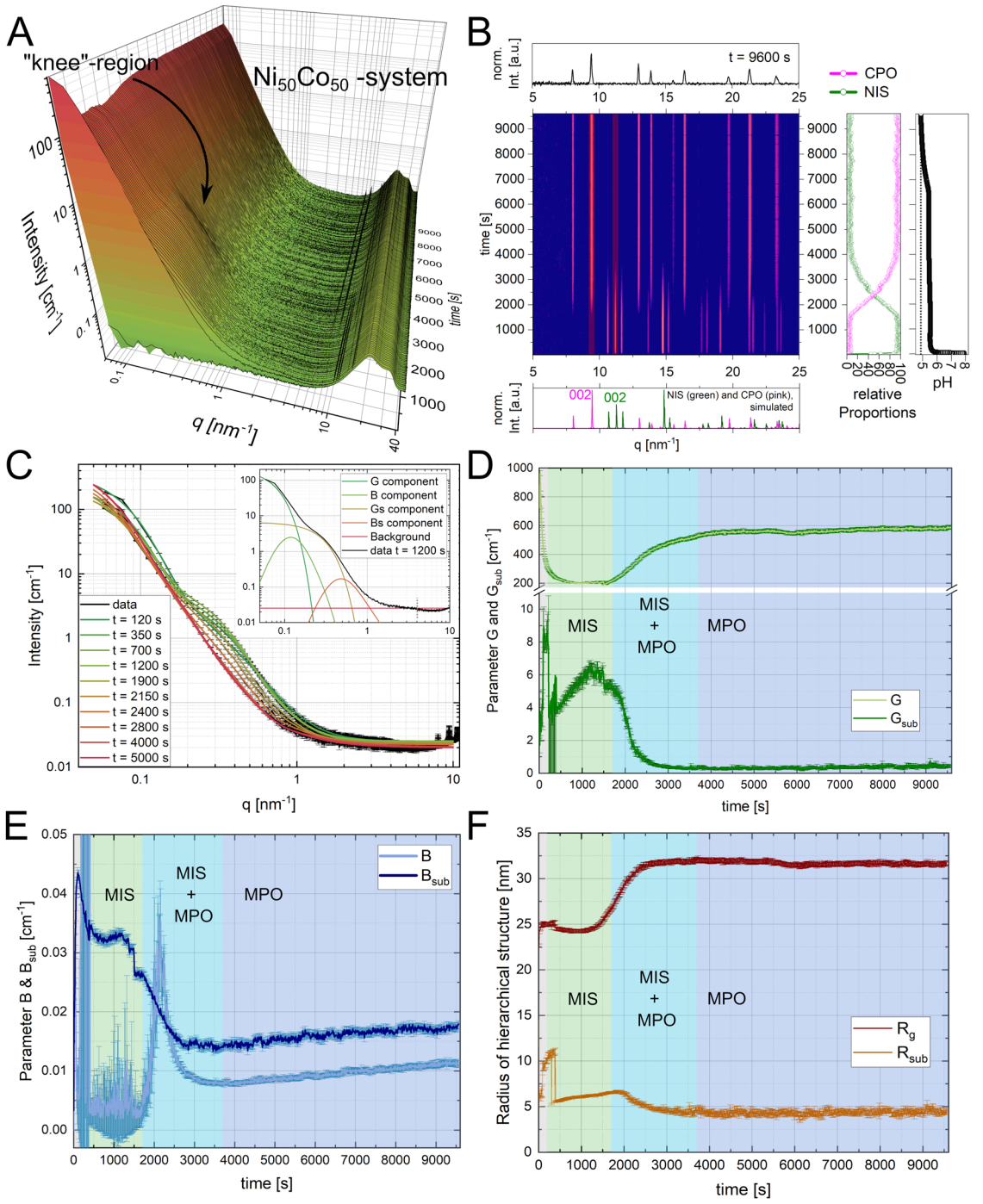

Figure 4. *In situ* scattering data and fits of the mixed $Ni_{50}Co_{50}$ system: (A) Time-resolved *in situ* SAXS data with color-marked intensities: low-intensity SAXS curves at the beginning represent the premixed stage of the pure DAP solution before injection of the metal-bearing solution. (B) WAXS heatmaps: normalized WAXS intensities plotted with simulated crystal structures and the final WAXS signal of the experiment. On the right side: normalized intensity of a characteristic (002) reflection of crystalline phase and simultaneously measured *in situ* pH data with the final equilibrated pH of the experiment marked by the dotted line (NIS = Ni-struvite, CPO = Co-phosphate octahydrate) marked with a red-shadowed frame. The relative proportions are normalized solely on the crystalline phases due to the presence of diffraction reflections. Ni-struvite reference ICSD 403058, Co-phosphate octahydrate COD reference 2020362.SAXS data: Projection of time-resolved normalized SAXS data with colored intensity. (C–F) Fitting results of the *in situ* SAXS data of the $Ni_{50}Co_{50}$ experiment based on a Beaucage model (Supporting Note 2, eq S1); (C) selected fits are displayed and show a good agreement with the data within the error bars; inset: component analysis of the fitting function following eq S1. Temporal evolutions of selected fitting parameters are presented in the panels (D–F): (D) G and G_{sub} and (E) B and B_{sub}. (F) R_g and R_{sub} in [nm]. The different color shadings mark the distinct phase composition at a given time based on WAXS: gray = no crystalline phases, light green = MIS (Ni_xCo_{1-x}-struvite), blue = MPO (M-phosphate octahydrate), cyan = both.

curves at low q near 0.1 nm^{-1} (affecting G) and the broad "hump" at around 0.4 nm^{-1} (affecting G_{sub}) (SI, Figure S8). After the formation of Ni-struvite crystals, all parameters reach a plateau value (SI, Figure S8).

https://doi.org/10.1021/acs.chemmater.3c02346
Chem. Mater. 2023, 35, 10645−10657

In contrast, in the Co system (SI, Figure S9), the presence of persisting long-lived amorphous phases manifested itself by increasing G, B_{sub}, and G_{sub} values, indicative of the presence of small building blocks and their agglomerates up to t = 500 s (SI, Figure S9). After t = 500 s, these parameters decrease sharply, correlating with the development of diffraction reflections, which correspond to Co-octahydrate. This suggests that crystallization is driven by the consumption of the amorphous phases. Indeed, we observed the coexistence of amorphous phases together with crystals in cryo-TEM analysis (Figure 2). We hypothesize an occurrence of the dissolution−reprecipitation process between the amorphous precursor and the crystalline phase, as the amorphous intermediates appear only in an agglomerated form and are absent at the interface of the crystal. As a result, the crystal most likely forms in the solution rather than in the amorphous framework, and therefore, it is isolated from the amorphous intermediates. After around t = 600 s, a plateau value is reached in most parameters, indicating the equilibration of the precipitation process.

Interestingly, when both metals, *i.e.*, Co and Ni, are mixed, the crystallization pathways become even more complex, deviating from the individual trends characteristic of the pure systems. Ni-struvite crystals formed fast within t < 100 s, while Co-phosphate octahydrate crystals were first observed after t > 600 s. Although we observed slightly contrasting kinetics among the used approaches (*e.g.*, see time axis in SI, Figure S2 and (Ni) Figure S8/(Co) Figure S9), the differences can be explained by changes in the hydrodynamic regime between the setups (confinement, pumping rate, *etc.*). We can conclude that Ni-phosphate demonstrates crystallization and transformation kinetics significantly faster than Co-phosphate. However, both elements precipitate into analogous struvite crystal structures, at least at low M/P ratios, although the pathways are clearly not identical. The Co system is potentially affected by the presence of long-living metal clusters, indicated by the long-term plateau value in pH at 5.7 and the delayed color change of the solution (Figures 2A and S2). The question arose as to how a mixed-metal system evolves toward crystalline solid solutions. We initially hypothesized that the development rate would be within the limits established by the pure-metal systems. As a result, compositions containing more Ni develop faster than those with more Co.

In contrast, the time for completion of the reaction increased strongly and differed significantly from the behavior of the two individual end members. We considered several Ni/Co ratios (Ni# = 20, 50, 80) at several concentrations (c(M) = 0.02 0.1, 1 M). In this regard, the most counterintuitive mixture was the 50:50 one that exhibited the longest equilibration times (SI, Figure S2E). This anomalous nonlinear (related to the Ni#) trend is further pronounced at very high concentrations of 1 M of the reactants, where the $Ni_{0.5}Co_{0.5}$ system required 6 h to complete, while the pure end members needed, at most, less than one-quarter of this time (SI, Figure S2E,F). The case of the $Ni_{50}Co_{50}$ mixture with its counterintuitively long reaction time (SI, Figure S2E,F) raised the question of how the reconfiguration of the precursor to a final crystalline unit was accomplished in this system. For this purpose, the $Ni_{50}Co_{50}$ system was also studied with *in situ* scattering accompanied by pH measurements to observe potential differences in their crystallization pathway.

In theory, both metals can be incorporated into the crystalline phases considered to form solid solutions.[4,5] However, upon precipitation from aqueous solution, the starting aqueous ionic concentrations and the final metal composition in the crystals differ significantly. Therefore, the occurring crystalline phases are named M-struvite and M-octahydrate with M = Ni_xCo_{1-x}. In the mixed system, surprisingly, the overall time scales of the entire formation process got extended significantly, and in addition, more complex transformation pathways were observed, including several crystalline phases. First, even faster than in the case of the Ni system, M-struvite formed within t = 100 s as observed in diffraction and correlating well with the occurrence of q^{-4} interfaces at low angles (Figure 4B). Simultaneously, coexisting amorphous phases scattered in the intermediate q region in a "knee" region at around 0.3−1 nm^{-1} similar to the pure Co system (Figures 3C and 4A). These scattering features of the amorphous phases evolved through time, reaching an intensity maximum at t = 1300 s. In the time interval from 1300 s < t < 1700 s, until the first formation of M-octahydrate, the signal at intermediate q decreased rapidly. In the time window from t = 1700−3700 s, the previously formed M-struvite and the M-octahydrate crystals coexisted. Here, the octahydrate's diffraction intensities increased further, indicative of a growing volume fraction of this phase, while the M-struvite crystals dissolved gradually, as evidenced by the disappearance of the associated Bragg peaks. After t = 3700 s, M-struvite was dissolved completely, resulting in a single-phase composition of M-octahydrate. Based on the pH curve, equilibrium was reached after the precipitation of M-octahydrate hinted by a drop of pH beginning at t = 6500 s finalized at t = 9000 s to reach a plateau value of 4.7. All significant events in the *in situ* scattering of the $Ni_{50}Co_{50}$ experiment are summarized in selective time frames (SI, Figure S7).

In the $Ni_{50}Co_{50}$ system, complex trends of the fitting parameters can be observed (Figures 4 and S10). First, at around t = 100 s, the sublevel parameters reached their maximum values (G_{sub} = 9 cm^{-1}, B_{sub} = 0.044 cm^{-1}, and R_{sub} = 11 nm), indicative of reaching a maximum number of nucleating entities with several nanometers in size (SI, Figure S10). Due to the partial consumption of these building blocks in the Ni-struvite crystal formation, all subparameters decreased roughly by half until t = 400 s (G_{sub} = 4 cm^{-1}, B_{sub} = 0.033 cm^{-1}, and R_{sub} = 5.5 nm, SI, Figure S10). In contrast, the hierarchically higher-level parameters G, B, and R_g declined rapidly to a minimum value (G = 200 cm^{-1}, B = 0.005 cm^{-1}, and R_g = 24 nm). Concurrently, the R_{sub} of the nucleating entities grew progressively by around 15% to around 7 nm until t = 1900 s (Figure 4F). When the dissolution of M-struvite (MIS) started, all subparameters declined to a global minimum. As R_{sub} most likely represents the radius of the smallest characteristic entity, it also declined to a constant plateau value. It is just affected by B_{sub} ($G_{sub} \approx 0$ cm^{-1}) and, therefore, the signal extinguishes after their consumption. Consequently, the evolution and absolute values of R_g are congruent and on the same length scale as the sizes of the spherical building units observable in the TEM micrographs. Due to the simultaneous coprecipitation of M-phosphate octahydrate (MPO), the higher-level parameters G and R_g increased to a plateau value with R_g = 32 nm and G = 580 cm^{-1} at around t = 3000 s. Most likely, even larger particles formed could not be quantified sufficiently well from the model, as the lower q-range would be required. B is deviating from this trend as it is affected by R_g and R_{sub} (SI, Supporting Note 2).

In sum, the fits of the *in situ* SAXS data reflect the nucleation of the precursors, its entities, and the transformation processes among them. The *in situ* scattering data demonstrate the

https://doi.org/10.1021/acs.chemmater.3c02346
Chem. Mater. 2023, 35, 10645−10657

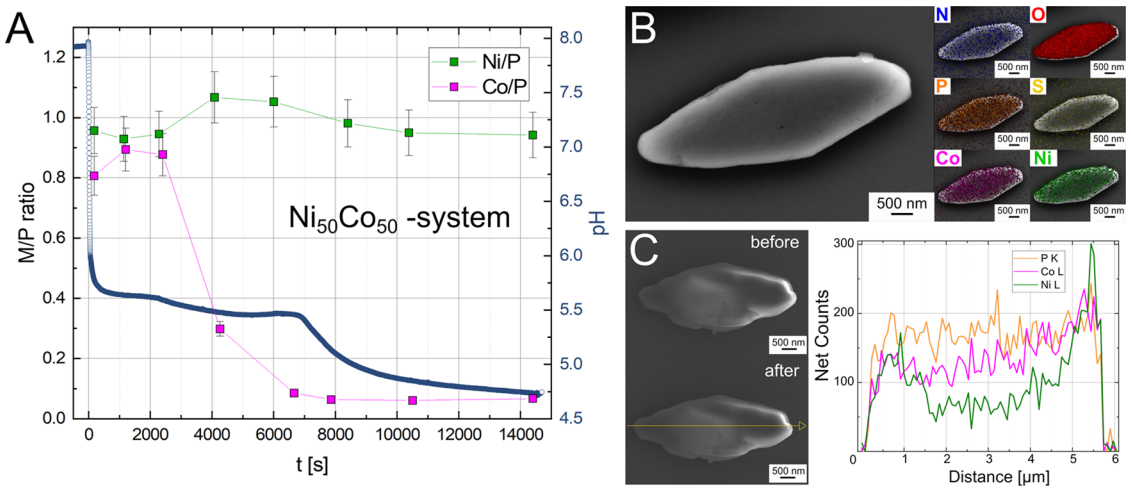

Figure 5. (A) *Ex situ* ICP-MS data plots of the supernatant (solution) displayed in mass ratios Ni/P and Co/P with the uncertainty of two standard deviations (95.7%) and simultaneously measured *in situ* pH curve. (B) SEM/EDS elemental maps and (C) SEM/EDS line scan of a single crystal of $Ni_xCo_{1-x}(PO_4)_2{\cdot}8H_2O$ with the elemental distribution of N, O, P, S, Co, and Ni, and SE images before and after the measurement.

coexistence of amorphous precursors and already formed crystalline phases over several time intervals.

In the pure-metal system, we observed a progressive transformation from amorphous to crystalline compounds. Based on this finding, we assumed that the formed crystals were the thermodynamically favored phases, *i.e.*, Ni- or Co-struvite. However, the mixed Ni_xCo_{1-x} experiments showed the opposite. Here, amorphous precursors coexist with crystalline phases over a long period, while the first precipitated crystals are unstable and "consumed" by a later forming crystalline phase.

Our results suggest that the reaction pathway is controlled by the type and concentration of the transition metal cation(s). Ni and Co can form the same isostructural crystalline phases, namely, M-struvite and M-octahydrate. Therefore, looking at the final crystalline solids, one would also expect isostructural TMP solid solutions that include both metals. However, the observed complex nonclassical crystallization pathways of the considered TMPs suggest that the incorporation of both metals into crystals would be driven by very different kinetic rates and thermodynamic equilibria of different multistep mechanisms. In this regard, the starting concentration of metals in solution is unlikely to reflect the metal concentration in the crystalline phases. Considering this hypothesis, in the further characterization, we explored if indeed any elemental fractionation occurred in the mixed Ni_xCo_{1-x} experiments between Ni and Co in their solid solutions. Therefore, to explain this aspect and to quantify the temporal elemental participation of P, Co, and Ni during the precipitation, we analyzed the chemical composition of the solid phases and the associated supernatants from different stages with ICP-MS. Although the measurements were essentially *ex situ*, we used the same flow-through setup as with the scattering experiments to synthesize TMPs to ensure near-direct comparability among various approaches, evidenced also by matching the pH trends (SI, Figure S11 and Table S3).

The ICP-MS data of the mother supernatant correlate with the observations of the *in situ* experiments (Figures 4 and 5A and Table S3). In the first seconds, Ni- and Co-PO_4 coprecipitated nearly equally, as it is visible in comparable MP ratios of around 0.9 (Figure 5A). From scattering, we learned that M-struvite formed quickly, while the amorphous phases began to agglomerate (Figures 3 and 4 and Table S3). Until around t = 3000 s, the Ni/P remained constant, while the Co/P ratio showed a slight increase of around 10% overall (Figure 5A). In this period, M-struvite and amorphous nanophases formed, as was indicated by the plateau value of the pH and the increasing sublevel parameters in scattering (Figures 4, S1−S3 and Table S3). After t = 3000 s, the simultaneous dissolution of the primary M-struvite and the precipitation of M-phosphate octahydrate resulted in a slightly increasing Ni/P ratio and starkly falling Co/P ratio (Figure 5A). The pH decreased slightly by 0.05, most likely due to the combined effect of the crystallization of M-phosphate octahydrate (causing a decrease in pH) and the release of PO_4^{3-} ions by dissolution of the as-formed M-struvite (leading to an increase in pH, see slightly higher absolute P mass ratio in the SI, Figure S11). Based on the increasing G and R_g scattering parameters and the elemental analysis, the formation of the M-phosphate octahydrate crystals occurred gradually over 2000−3000 s. At this stage, Ni was released slightly ≈+15% into the solution, resulting in a Ni/P ratio of ≈1.05, while Co was almost completely ≈−90% (decreasing Co/P ratio in the solution ≈0.05) incorporated in a solid phase (Figure 5A). Importantly, M-phosphate octahydrate had a higher MP = 1.5 than M-struvite with MP = 1, and therefore, the absolute phosphate content increased after dissolution of M-struvite. Finally, after extended reaction times of t = 8000 s, the Ni/P ratio declined to a constant value of 0.9, reflecting only a partial incorporation of Ni into the M-phosphate octahydrate crystals. Most of the Co content was precipitated in $M_3(PO_4)_2{\cdot}8H_2O$ crystals, resulting in a low remaining absolute Co content in the solution. Based on the EDS mappings, line scans, and bulk ICP-MS data from different Ni_xCo_{1-x} mixtures (x = 0.3, 0.5, and 0.7), we observed an extensive trend of metal fractionation during the formation of M-phosphate octahydrate (Figure 5B). The calculated Ni# from EDS analysis of the mapped $M_3(PO_4)_2{\cdot}8H_2O$ crystals was significantly lower than Ni# in the solution (SI, Figure S14). Furthermore, in the EDS line scans, a slight zonation of Ni in the Co-rich samples could be identified (Ni# > 0.5) in the M-phosphate octahydrate crystals (Figure 5C). Here, Ni was concentrated in the outer rims, while the cores of the crystals were enriched in Co, respectively, to each other (Figure 5C). In addition, the calculated Ni# from bulk ICP-MS data agreed well with the EDS data (SI, Table S4). Thus, the fractionation of Ni and Co occurred in all crystals following the same temporal and spatial patterns of the elemental distribution.

https://doi.org/10.1021/acs.chemmater.3c02346
Chem. Mater. 2023, 35, 10645−10657

Interestingly, in the Ni_xCo_{1-x} mixture with $x = 0.8$, where M-struvite was also present at the end of the reaction with M-phosphate octahydrate in a binary phase mixture (SI, Figure S1), the calculated Ni# agreed with the Ni# in the solution (SI, Figures S13, S14 and Table S2).

Interestingly, the secondary decrease in pH from around 5.4 to 4.7 (ΔpH = 0.7) for $t > 7000$ s was observed in the pure Co and mixed Ni_xCo_{1-x} system at higher concentrations $c(M^{2+}) > 0.6$ M. This pH drop occurred already after the color change or the first occurrence of diffraction reflections from the M-phosphate octahydrate. Consequently, this second pH drop is most likely caused by the progressive crystallization of the M-phosphate octahydrate. In the pH range of 7 to 5, where the crystallization process starts, $H_2PO_4^-$ is the most abundant phosphate species. In the first step, these hydrogen phosphate units carrying hydroxyl groups are probably incorporated into the crystal structure of M-phosphate octahydrate when the initial crystallization starts. In a second step after the initial crystallization, we assume that the hydroxyl groups release their protons, resulting in a secondary pH drop toward the final equilibrium. Moreover, we can exclude a significant effect of ammonium in this step as this pH drop also occurred in the reaction runs with another phosphate precursor, *e.g.*, Na_2HPO_4 (SI, Figure S2D).

Transformation of the Amorphous Precursor and Reaction Kinetics of Transition Metals. The occurrence of intermediate amorphous nanophases in the pure- and mixed-metal systems, followed by their restructuring and densification, demonstrated a multistep crystallization route. Therefore, the TMP crystallization is nonclassical. Although the amorphous intermediate phases formed quickly in the early reaction stages, their reconfiguration and aggregation occurred gradually over many seconds to minutes. After a threshold density and micrometer size of the agglomerates were reached, the final transformation to a crystal seemed to be very fast. Since the actual transformation to a crystalline material occurred within seconds and exhibited highly stochastic characteristics, it proved challenging to be tracked with *ex situ* approaches. Namely, transitional amorphous phases and final crystals can coexist within a limited metastable time window. Interestingly, neither individual nanocrystals nor standalone spherical building units were found in the samples. Instead, we observed only larger mesoscopic agglomerates of building units or already crystals of μm size. This suggests that the outcome of TMP crystallization should be potentially controllable by confinement/finite volume.[59] We speculate that the occurrence and the stability of the amorphous phases are actually controlled by metastable, but long-living, aqua ammonia complexes $(M^{2+}(H_2O)_x(NH_3)_{1-x})$ present in solutions, whose evolution affects the equilibria of the evolving solids.[60,61] They may have an impact on crystallization, *i.e.*, on the formation of nanometer-sized clusters by decreasing the amount of available free Ni^{2+}, Co^{2+}, or NH_4^+ ions. Such speciation-dependent, solid *vs* aqueous cluster equilibria would explain very different transformation kinetics of the amorphous phase agglomerates, including the anomalous evolution in the mixed-metal systems. Another kinetic reason to consider, in light of the evolution of pH trends, is associated stabilities of different protonated phosphate species. Starting pH $\approx$ 8, such conditions would stabilize predominantly the single-protonated HPO_4^{2-} species, while at the end of precipitation, the drop in pH to 4.6 would shift the equilibrium to the double protonated $H_2PO_4^-$. The presence of different protonated phosphate ligands in an aqueous solution could potentially affect the local structure of strongly hydrated amorphous transition metal phosphate nanophases, analogously observed in calcium carbonate and calcium phosphate systems.[62−64] They could form similar frameworks as observed structures of Posner clusters in the crystallization pathway of apatite.[65,66]

Growth of Crystalline Phases. Since the TMP crystallization pathways are multistep, consequently, the reaction kinetics of the TMP precipitation is primarily dependent on the stability of the amorphous precursors and their agglomerates, and to a lesser extent on the final crystallization step. However, this "final" transformation ought to be also considered. Looking at the solubility product, *i.e.*, the thermodynamic driving force for precipitation, the K_{sp} of M-struvite is orders of magnitudes higher than that of M-phosphate octahydrate at ambient conditions.[67,68] However, M-struvite still demonstrates faster reaction kinetics compared to M-phosphate octahydrate. This could be explained by crystallographic differences in the transition metal phosphate structures. Based on the cryo-TEM and *in situ* scattering data, we could indeed extract the information about phase, morphology, and key differences in the evolving frameworks of the amorphous phases and their transformation to crystalline solids depending on the involved transition metals. While we focused in the previous part of the discussion on the stability and the effects of the amorphous phases, we consider further the evolution of the occurring crystal structures, namely, M-struvite and M-phosphate octahydrate. From a crystallographic standpoint, as Co-phosphate octahydrate exhibits large d_{hkl} of the (110) and (002) plane, due to its layered structure (Figures 3 and 4, q_{110} or $q_{002} < 10$ nm^{-1}), these crystal planes exhibit the resulting high load densities and growth velocities. This is the reason why these planes have a large probability of forming and scattering with high intensity (as is concluded from the Bravais−Friedel−Donnay−Harker model).[69,70] As can be seen in Figure 3, in M-struvite, the intensity of the (101), (002), and (011) reflections increases immediately, while the (110) and (020) reflections of M-phosphate octahydrate grow gradually due to their layered nature. The fast formation kinetics of M-struvite compared to M-phosphate octahydrate are probably related to its simple crystallographic structure of isolated building units, mainly the isolated phosphate tetrahedron and isolated metal octahedron coordinated by crystal water.[4,54,71] However, the Co-phosphate octahydrate structure is more complex, depicted, for example, in the occurrence of two different metal sites. In the first site, the transition metal is surrounded by four water molecules and two oxygen atoms, resulting in the octahedron $Co(H_2O)_4O_2$. In the second site, the transition metal is coordinated by two water molecules and four oxygen atoms, leading to $Co(H_2O)_2O_4$. The (110) reflection of M-phosphate octahydrate represents the crystal plane constructed by a regular arrangement of octahedral $Co(H_2O)_4O_2$ or $Co(H_2O)_2O_4$ units with a *d*-spacing of $d_{110} = 7.83$ Å, whereas the (020) reflection lies in the plane of linked Co octahedrons (both types) with tetrahedral-coordinated PO_4 phosphate units with a *d*-spacing of $d_{020} = 6.67$ Å. First, the crystal structure is most likely to build up in one c-layer by the arrangement of disordered super units of linked Co octahedrons and PO_4 tetrahedrons, resulting in the presence of the (110) and (020) reflections. Here, 001 reflections would not occur as the layers are internally disordered and grow in single layers. At extended reaction time, additional layers begin to form in the *c*-direction. Here, inside the c-layer, $Co(H_2O)_4O_2$ and PO_4 self-assemble and reach a higher degree of ordering, resulting in the

https://doi.org/10.1021/acs.chemmater.3c02346
Chem. Mater. 2023, 35, 10645−10657

appearance of (200) [d_{200} = 4.84 Å], (001) [d_{001} = 4.52 Å] and other reflections. A visualization of the lattice planes in the crystal structure of Co-phosphate octahydrate is depicted in the SI (Figure S15).

The actual accomplishment of the transformation in the solid compounds, from a disordered, amorphous to an ordered, crystalline state, is still not fully understood, either in phosphates or in other mineral systems. For instance, this issue of a stochastic "jump" of a dense agglomerate to a primary crystal is also debated[62,72,73] in other material classes, such as the conversion of amorphous calcium carbonate (ACC) to a crystalline carbonate[74,75] or in the calcium sulfate system.[51] However, we hypothesize the presence of a dissolution−reprecipitation process along the phase transition between amorphous and crystalline transition metal phosphates. Indicators for this assumption in the pure Ni- or Co-PO_4 system are the decrease in intensities in the *in situ* scattering experiments and the decreasing electron density contrast of the amorphous precursors in the cryo-TEM micrographs. In all time steps of the cryo-approach, we observed them in an agglomerated framework, but not as isolated single-building units. In addition, no amorphous phases were found in the proximity of the crystalline facets of the crystals for extended reaction times (Ni: t = 900 s, Co: t = 2100 s). Thus, the primary nucleating crystal forms in the solution. In the mixed Ni_xCo_{1-x} system, the phase transition mechanism could deviate significantly from the pure endmembers as multiple metastable amorphous and crystalline phases coexist in a limited time window. Therefore, we cannot exclude other phase transition mechanisms, *e.g.*, as solid−solid phase transition for the mixed Ni_xCo_{1-x} system. Although a dissolution−reprecipitation process was most likely the primary mechanism, an extensive process of agglomeration and densification of the amorphous precursors took place at different time scales, from minutes to hours, before their actual dissolution/transformation to a crystal.

CONCLUSIONS

We revealed how transition metal phosphates form crystals through a nonclassical pathway that involves temporary, amorphous particles on the way to the final crystal. These amorphous phases undergo various stages of aggregation, densification, and reconfiguration to protocrystalline precursors varying considerably depending on the transition metal(s) involved. The reaction kinetics of the precipitation of TMP phases is primarily dependent on the involved transition metal(s), the stability properties of the amorphous precursors, and their agglomerated entities. Additionally, the rate of formation is affected by the complexity of the final crystalline structure (layered *vs* isolated structure). When combining Ni and Co equally in high concentration, the time it took to reach equilibrium was significantly prolonged, from a few minutes to several hours, providing evidence of the intricate interaction between transition metal ions and potential complexes and the nucleating solid entities.

ASSOCIATED CONTENT

Data Availability Statement

Additional data that support the findings of this study are available from the corresponding authors upon reasonable request.

Supporting Information

The Supporting Information is available free of charge at https://pubs.acs.org/doi/10.1021/acs.chemmater.3c02346.

3D tomographic reconstruction of the Ni-PO_4 precursor phases at t = 300 s derived from cryo-TEM micrographs is shown in different orientations (−60° < θ < 60°), 360° rotation of the reconstructed object around the z-axis in the x−y-plane (Video S1) (AVI)

3D tomographic reconstruction of the Co-PO_4 precursor phases at t = 600 s, derived from cryo-TEM micrographs is shown in different orientations (−60° < θ < 60°), 360° rotation of the reconstructed object around the z-axis in the x−y-plane (Video S2) (AVI)

Time-resolved pH data of the one-pot synthesis and the *in situ* scattering experiments are attached in the csv files, for the *in situ* scattering experiments, the phase fraction curves of the crystalline phases can be found in absolute and normalized values (pH_measurements_Onepotsynthesis.csv, *in situ*_data_Co.csv, *in situ*_data_Ni.csv, *in situ*_data_NiCo.csv) (ZIP)

X-ray diffraction; pH measurements; infrared spectroscopy; SEM/EDS; conventional TEM; Cryo-TEM; *in situ* SAXS/WAXS; ICP-MS (Methods); stacked diffractograms of synthesized Ni, Co, and Ni_xCo_{1-x} phosphate samples (Figure S1); time-resolved pH data of different reaction runs of Ni, Co, and Ni_xCo_{1-x} with x = 20, 50, 80% phosphates in varying concentrations (Figure S2); conventional TEM micrographs of Ni- and Co phosphates with BF image and associated EDX maps of the precursor Ni- or Co-phosphate phases (Figure S3); Cryo-TEM analysis and tomographic reconstructions of the amorphous Ni and Co phosphate nanophases displayed in different angles (Figure S4); Fourier transform-infrared (FT-IR) spectra of crystalline Ni_xCo_{1-x}- samples (Figure S5); flow-through-setup sketch (Figure S6); selected time frames in scattering/diffraction of the mixed $Ni_{50}Co_{50}$ experiment and component analysis of the fit function (Figure S7); fitting results of the *in situ* SAXS data of the Ni-experiment based on a Beaucage model (Figure S8); fitting results of the *in situ* SAXS data of the Co-experiment based on a Beaucage model (Figure S9); fitting results of the *in situ* SAXS data of the mixed $Ni_{50}Co_{50}$-experiment based on a Beaucage model (Figure S10); ICP-MS data of the particle-filtered solution with triplicate runs in absolute mass fractions (Figure S11); EDS maps of analyzed Ni_xCo_{1-x} solids with x = 0.1−0.9 (Figure S12); EDS Line Scans of analyzed Ni_xCo_{1-x} solids with x = 30, x = 50 and x = 80 in the experiment (Figure S13); ICP-MS data of Ni, Co and P and comparison of elemental information obtained by ICP-MS and the EDX maps of multiple grains (Figure S14); crystal structures of M-struvite *Pmn*21 and M-phosphate octahydrate *C*2/m (Figure S15); settings of the ICP-MS instrument used for the quantification (Table S1); summarized EDS data from multiple maps of Ni_xCo_{1-x}-phosphate octahydrate crystals with weight and atomic percentage of the respective element (Table S2); ICP-MS data of particle-filtered solution from crystallization experiments in triplicate runs (Table S3); ICP-MS data of dissolved $(Ni_xCo_{1-x})3(PO_4)_2$ crystals in triplicate runs (Table S4); pH curves as a proxy for reaction progress (Supporting Note 1); fitting SAXS data

https://doi.org/10.1021/acs.chemmater.3c02346
Chem. Mater. 2023, 35, 10645−10657

with a simplified Beaucage model (Supplorting Note 2) (PDF)

AUTHOR INFORMATION

Corresponding Authors

Tomasz M. Stawski − *Federal Institute for Materials Research and Testing, Berlin 12489, Germany;* orcid.org/0000-0002-0881-5808; Email: tomasz.stawski@bam.de

Stephanos Karafiludis − *Federal Institute for Materials Research and Testing, Berlin 12489, Germany; Department of Chemistry, Humboldt-Universität zu Berlin, Berlin 12489, Germany*; Email: stephanos.karafiludis@bam.de

Authors

Zdravko Kochovski − *Department for Electrochemical Energy Storage, Helmholtz-Zentrum Berlin for Materials and Energy, Berlin 14109, Germany;* orcid.org/0000-0001-8375-0365

Ernesto Scoppola − *Biomaterials, Hierarchical Structure of Biological and Bio-inspired Materials, Max Planck Institute of Colloids and Interfaces, Potsdam 14476, Germany;* orcid.org/0000-0002-6390-052X

Anika Retzmann − *Federal Institute for Materials Research and Testing, Berlin 12489, Germany*

Vasile-Dan Hodoroaba − *Federal Institute for Materials Research and Testing, Berlin 12489, Germany;* orcid.org/0000-0002-7901-6114

Johan E. ten Elshof − *MESA+ Institute for Nanotechnology, University of Twente, Enschede 7500 AE, The Netherlands;* orcid.org/0000-0001-7995-6571

Franziska Emmerling − *Federal Institute for Materials Research and Testing, Berlin 12489, Germany; Department of Chemistry, Humboldt-Universität zu Berlin, Berlin 12489, Germany;* orcid.org/0000-0001-8528-0301

Complete contact information is available at: https://pubs.acs.org/10.1021/acs.chemmater.3c02346

Notes

The authors declare no competing financial interest.

ACKNOWLEDGMENTS

The authors thank BAM and Helmholtz-Zentrum Berlin (HZB) for providing beamtime at mySpot of BESSY II. In addition, they thank Helmholtz-Zentrum Berlin (HZB) for providing access to the electron microscopes.

REFERENCES

(1) Gislev, M.; Grohol, M.; Mathieux, F.; Ardente, F. *Report on Critical Raw Materials in the Circular Economy*, European Commission2018.

(2) Cordell, D.; Drangert, J.-O.; White, S. The story of phosphorus: Global food security and food for thought. *Global Environ. Change* **2009**, *19* (2), 292−305.

(3) Filippelli, G. M. The Global Phosphorus Cycle. *Rev. Mineral. Geochem.* **2002**, *48* (1), 391−425.

(4) Karafiludis, S.; Buzanich, A.G.; Kochovski, Z.; Feldmann, I.; Emmerling, F.; Stawski, T. M. Ni- and Co-Struvites: Revealing Crystallization Mechanisms and Crystal Engineering toward Applicational Use of Transition Metal Phosphates. *Cryst. Growth Des.* **2022**, *22* (7), 4305−4315.

(5) Karafiludis, S.; Buzanich, A. G.; Heinekamp, C.; Zimathies, A.; Smales, G. J.; Hodoroaba, V.-D.; ten Elshof, J. E.; Emmerling, F.; Stawski, T. M. Template-free synthesis of mesoporous, amorphous transition metal phosphate materials. *Nanoscale* **2023**, *15* (8), 3952−3966.

(6) Mohammed, H.; Al-Othman, A.; Nancarrow, P.; Elsayed, Y.; Tawalbeh, M. Enhanced proton conduction in zirconium phosphate/ionic liquids materials for high-temperature fuel cells. *Int. J. Hydrogen Energy* **2021**, *46* (6), 4857−4869.

(7) Huang, W.; Komarneni, S.; Noh, Y. D.; Ma, J.; Chen, K.; Xue, D.; Xue, X.; Jiang, B. Novel inorganic tin phosphate gel: multifunctional material. *Chem. Commun.* **2018**, *54* (21), 2682−2685.

(8) Karafiludis, S.; Bhattacharya, B.; Buzanich, A. G.; Fink, F.; Feldmann, I.; ten Elshof, J. E.; Emmerling, F.; Stawski, T. M. Thermally processed Ni-and Co-struvites as functional materials for proton conductivity. *Dalton Trans.* **2023**, *52* (24), 8262−8274.

(9) Zhao, Y.; Chen, Z.; Xiong, D.-B.; Qiao, Y.; Tang, Y.; Gao, F. Hybridized Phosphate with Ultrathin Nanoslices and Single Crystal Microplatelets for High Performance Supercapacitors. *Sci. Rep.* **2016**, *6*, No. 17613.

(10) Lin, J.; Chen, N.; Pan, Y. Arsenic incorporation in synthetic struvite ($NH_4MgPO_4{\cdot}6H_2O$): a synchrotron XAS and single-crystal EPR study. *Environ. Sci. Technol.* **2013**, *47* (22), 12728−12735.

(11) Xu, X.; Du, P.; Guo, T.; Zhao, B.; Wang, H.; Huang, M. In situ Grown Ni phosphate@Ni12P5 Nanorod Arrays as a Unique Core−Shell Architecture: Competitive Bifunctional Electrocatalysts for Urea Electrolysis at Large Current Densities. *ACS Sustainable Chem. Eng.* **2020**, *8* (19), 7463−7471.

(12) Meguerdichian, A. G.; Jafari, T.; Shakil, M. R.; Miao, R.; Achola, L. A.; Macharia, J.; Shirazi-Amin, A.; Suib, S. L. Synthesis and Electrocatalytic Activity of Ammonium Nickel Phosphate, $[NH_4]$-$NiPO_4{\cdot}6H_2O$, and beta-Nickel Pyrophosphate, beta-$Ni_2P_2O_7$: Catalysts for Electrocatalytic Decomposition of Urea. *Inorg. Chem.* **2018**, *57* (4), 1815−1823.

(13) Septiani, N. L. W.; Kaneti, Y. V.; Fathoni, K. B.; Kani, K.; Allah, A. E.; Yuliarto, B.; Nugraha; Dipojono, H. K.; Alothman, Z. A.; Golberg, D.; Yamauchi, Y. Self-Assembly of Two-Dimensional Bimetallic Nickel−Cobalt Phosphate Nanoplates into One-Dimensional Porous Chainlike Architecture for Efficient Oxygen Evolution Reaction. *Chem. Mater.* **2020**, *32* (16), 7005−7018.

(14) Song, Z.; Wang, K. C.; Sun, Q.; Zhang, L.; Li, J.; Li, D.; Sze, P. W.; Liang, Y.; Sun, X.; Fu, X. Z.; Luo, J. L. High-Performance Ammonium Cobalt Phosphate Nanosheet Electrocatalyst for Alkaline Saline Water Oxidation. *Adv. Sci.* **2021**, *8* (14), No. 2100498.

(15) Zhao, H.; Yuan, Z.-Y. Insights into Transition Metal Phosphate Materials for Efficient Electrocatalysis. *ChemCatChem* **2020**, *12* (15), 3797−3810.

(16) Lin, R.; Ding, Y. A Review on the Synthesis and Applications of Mesostructured Transition Metal Phosphates. *Materials* **2013**, *6* (1), 217−243.

(17) Huang, H.; Xu, C.; Zhang, W. Removal of nutrients from piggery wastewater using struvite precipitation and pyrogenation technology. *Bioresour. Technol.* **2011**, *102* (3), 2528−2523.

(18) El Diwani, G.; El Rafie, S.; El Ibiari, N. N.; El-Aila, H. I. Recovery of ammonia nitrogen from industrial wastewater treatment as struvite slow releasing fertilizer. *Desalination* **2007**, *214* (1−3), 200−214.

(19) Münch, E. V.; Barr, K. Controlled struvite crystallisation for removing phosphorus from anaerobic digester sidestreams. *Water Res.* **2001**, *35* (1), 151−159.

(20) Paskin, A.; Couasnon, T.; Perez, J. P. H.; Lobanov, S. S.; Blukis, R.; Reinsch, S.; Benning, L. G. Nucleation and Crystallization of Ferrous Phosphate Hydrate via an Amorphous Intermediate. *J. Am. Chem. Soc.* **2023**, *145* (28), 15137−15151.

(21) Zhangchen, R.; Liu, W.; G, Q.; Ji, H.; Li, Y.; Zhang, J.; Song, J.; Zhong, Y.; Zhou, L. Struvite as seed materials for treatment of heavy metals in wastewater. *IOP Conf. Ser.: Earth Environ. Sci.* **2021**, *770*, No. 012034.

(22) Rouff, A. A. Sorption of chromium with struvite during phosphorus recovery. *Environ. Sci. Technol.* **2012**, *46* (22), 12493−12501.

(23) Rouff, A. A.; Juarez, K. M. Zinc interaction with struvite during and after mineral formation. *Environ. Sci. Technol.* **2014**, *48* (11), 6342−6349.

(24) Lu, X.; Huang, Z.; Liang, Z.; Li, Z.; Yang, J.; Wang, Y.; Wang, F. Co-precipitation of Cu and Zn in precipitation of struvite. *Sci. Total Environ.* **2021**, *764*, No. 144269.
(25) Ravikumar, R.; Chandrasekhar, A.; Krishnar, C. R.; Reddy, Y. X-ray powder diffraction, thermal analysis and IR studies of zinc ammonium phosphate hexahydrate. *Optoelectron. Adv. Mater.* **2010**, *4*, 215−219.
(26) Haferburg, G.; Kloess, G.; Schmitz, W.; Kothe, E. Ni-struvite" - a new biomineral formed by a nickel resistant Streptomyces acidiscabies. *Chemosphere* **2008**, *72* (3), 517−523.
(27) Abbona, F.; Angela-Franchini, M.; Croni Bono, C.; Lundager Madsen, H. E. Effect of ammonia excess on the crystal habit of $NiNH_4PO_4{\cdot}6H_2O$ (Ni-struvite). *J. Cryst. Growth* **1994**, *143* (3), 256−260.
(28) Hövelmann, J.; Stawski, T. M.; Freeman, H. M.; Besselink, R.; Mayanna, S.; Perez, J. P. H.; Hondow, N. S.; Benning, L. G. Struvite Crystallisation and the Effect of Co^{2+} Ions. *Minerals* **2019**, *9* (9), No. 503.
(29) Hövelmann, J.; Stawski, T. M.; Besselink, R.; Freeman, H. M.; Dietmann, K. M.; Mayanna, S.; Pauw, B. R.; Benning, L. G. A template-free and low temperature method for the synthesis of mesoporous magnesium phosphate with uniform pore structure and high surface area. *Nanoscale* **2019**, *11* (14), 6939−6951.
(30) Gibbs, J. W. On the Equilibrium of Heterogeneous Substances. *Trans. Conn. Acad. Arts Sci.* **1876**, *3*, 108−248.
(31) Volmer, M.; Weber, A. Keimbildung in übersättigten Gebilden. *Z. Phys. Chem.* **1926**, *119U*, 277−301.
(32) Lin, C.; Zhang, Y.; Liu, J. J.; Wang, X. Z. Study on nucleation kinetics of lysozyme crystallization. *J. Cryst. Growth* **2017**, *469*, 59−64.
(33) Auer, S.; Frenkel, D. Numerical prediction of absolute crystallization rates in hard-sphere colloids. *J. Chem. Phys.* **2004**, *120* (6), 3015−3029.
(34) Kalikmanov, V. I. Effective binary theory of multi-component nucleation. *J. Chem. Phys.* **2015**, *142* (12), No. 124111.
(35) Merikanto, J.; Zapadinsky, E.; Lauri, A.; Vehkamaki, H. Origin of the failure of classical nucleation theory: incorrect description of the smallest clusters. *Phys. Rev. Lett.* **2007**, *98* (14), No. 145702.
(36) Schmelzer, J. W. P.; Abyzov, A. S. Crystallization of glass-forming melts: New answers to old questions. *J. Non-Cryst. Solids* **2018**, *501*, 11−20.
(37) Gránásy, L.; Iglói, F. Comparison of experiments and modern theories of crystal nucleation. *J. Chem. Phys.* **1997**, *107*, 3634−3644.
(38) Oxtoby, D. W. Nucleation of First-Order Phase Transitions. *Acc. Chem. Res.* **1998**, *31* (2), 91−97.
(39) Gebauer, D.; Völkel, A.; Cölfen, H. Stable prenucleation Calcium Carbonate Clusters. *Science* **2008**, *322* (5909), 1819−1822.
(40) Vekilov, P. G. The two-step mechanism of nucleation of crystals in solution. *Nanoscale* **2010**, *2* (11), 2346−2357.
(41) Cookman, J.; Hamilton, V.; Hall, S. R.; Bangert, U. Non-classical crystallisation pathway directly observed for a pharmaceutical crystal via liquid phase electron microscopy. *Sci. Rep.* **2020**, *10* (1), No. 19156.
(42) Warzecha, M.; Florence, A. J.; Vekilov, P. G. The Ambiguous Functions of the Precursors That Enable Nonclassical Modes of Olanzapine Nucleation and Growth. *Crystals* **2021**, *11* (7), No. 738.
(43) Sauter, A.; Oelker, M.; Zocher, G.; Zhang, F.; Stehle, T.; Schreiber, F. Nonclassical Pathways of Protein Crystallization in the Presence of Multivalent Metal Ions. *Cryst. Growth Des.* **2014**, *14* (12), 6357−6366.
(44) Sauter, A.; Roosen-Runge, F.; Zhang, F.; Lotze, G.; Jacobs, R. M.; Schreiber, F. Real-time observation of nonclassical protein crystallization kinetics. *J. Am. Chem. Soc.* **2015**, *137* (4), 1485−1491.
(45) Sleutel, M.; Van Driessche, A. E. Role of clusters in nonclassical nucleation and growth of protein crystals. *Proc. Natl. Acad. Sci. U.S.A.* **2014**, *111* (5), E546−53.
(46) Greer, H. F. Non-classical crystal growth of inorganic and organic materials. *Mater. Sci. Technol.* **2014**, *30* (6), 611−626.
(47) Tsarfati, Y.; Rosenne, S.; Weissman, H.; Shimon, L. J. W.; Gur, D.; Palmer, B. A.; Rybtchinski, B. Crystallization of Organic Molecules: Nonclassical Mechanism Revealed by Direct Imaging. *ACS Cent. Sci.* **2018**, *4* (8), 1031−1036.
(48) Suk, J.-H.; Hwang, N.-M. Non-classical Crystallization of Bulk Crystals in Solution and of Thin Films in the Gas Phase by Chemical Vapor Deposition. *Electron. Mater. Lett.* **2022**, *18* (1), 1−26.
(49) Jung, J.-S.; Hwang, N.-M.Non-Classical Crystallization of Thin Films and Nanostructures in CVD Process. In *Chemical Vapor Deposition - Recent Advances and Applications in Optical, Solar Cells and Solid State Devices*; IntechOpen, 2016.
(50) Sear, R. P. The non-classical nucleation of crystals: microscopic mechanisms and applications to molecular crystals, ice and calcium carbonate. *Int. Mater. Rev.* **2012**, *57* (6), 328−356.
(51) Stawski, T. M.; van Driessche, A. E.; Ossorio, M.; Rodriguez-Blanco, J. D.; Besselink, R.; Benning, L. G. Formation of calcium sulfate through the aggregation of sub-3 nanometre primary species. *Nat. Commun.* **2016**, *7*, No. 11177.
(52) Ruiz-Agudo, E.; Ruiz-Agudo, C.; Di Lorenzo, F.; Alvarez-Lloret, P.; Ibanez-Velasco, A.; Rodriguez-Navarro, C. Citrate Stabilizes Hydroxylapatite Precursors: Implications for Bone Mineralization. *ACS Biomater. Sci. Eng.* **2021**, *7* (6), 2346−2357.
(53) Besselink, R.; Stawski, T. M.; Freeman, H. M.; Hövelmann, J.; Tobler, D. J.; Benning, L. G. Mechanism of Saponite Crystallization from a Rapidly Formed Amorphous Intermediate. *Cryst. Growth Des.* **2020**, *20* (5), 3365−3373.
(54) Karafiludis, S.; Ryll, T. W.; Guilherme Buzanich, A.; Emmerling, F.; Stawski, T. M. Phase stability studies on transition metal phosphates aided by an automated synthesis. *CrystEngComm* **2023**, *25* (30), 4333−4344.
(55) Midgley, P. A.; Dunin-Borkowski, R. E. Electron tomography and holography in materials science. *Nat. Mater.* **2009**, *8* (4), 271−280.
(56) Besselink, R.; Stawski, T. M.; Van Driessche, A. E. S.; Benning, L. G. Not just fractal surfaces, but surface fractal aggregates: Derivation of the expression for the structure factor and its applications. *J. Chem. Phys.* **2016**, *145* (21), No. 211908.
(57) Beaucage, G. Approximations Leading to a Unified Exponential/Power-Law Approach to Small-Angle Scattering. *J. Appl. Crystallogr.* **1995**, *28*, 717−728.
(58) Beaucage, G. Small-Angle Scattering from Polymeric Mass Fractals of Arbitrary Mass-Fractal Dimension. *J. Appl. Crystallogr.* **1996**, *29*, 134−146.
(59) Meldrum, F. C.; O'Shaughnessy, C. Crystallization in Confinement. *Adv. Mater.* **2020**, *32* (31), No. 2001068.
(60) van Bommel, A.; Dahn, J. R. Analysis of the Growth Mechanism of Coprecipitated Spherical and Dense Nickel, Manganese, and Cobalt-Containing Hydroxides in the Presence of Aqueous Ammonia. *Chem. Mater.* **2009**, *21* (8), 1500−1503.
(61) Rodríguez-Iznaga, I.; Petranovskii, V.; Rodríguez-Fuentes, G. Ion-exchange of amino- and aqua-complexes of nickel and cobalt in natural clinoptilolite. *J. Environ. Chem. Eng.* **2014**, *2* (3), 1221−1227.
(62) Wolf, S. E.; Muller, L.; Barrea, R.; Kampf, C. J.; Leiterer, J.; Panne, U.; Hoffmann, T.; Emmerling, F.; Tremel, W. Carbonate-coordinated metal complexes precede the formation of liquid amorphous mineral emulsions of divalent metal carbonates. *Nanoscale* **2011**, *3* (3), 1158−1165.
(63) Habraken, W. J. E. M.; Tao, J.; Brylka, L. J.; Friedrich, H.; Bertinetti, L.; Schenk, A. S.; Verch, A.; Dmitrovic, V.; Bomans, P. H.; Frederik, P. M.; Laven, J.; van der Schoot, P.; Aichmayer, B.; de With, G.; DeYoreo, J. J.; Sommerdijk, N. A. Ion-association complexes unite classical and non-classical theories for the biomimetic nucleation of calcium phosphate. *Nat. Commun.* **2013**, *4*, No. 1507.
(64) Lin, T. J.; Chiu, C. C. Structures and infrared spectra of calcium phosphate clusters by ab initio methods with implicit solvation models. *Phys. Chem. Chem. Phys.* **2018**, *20* (1), 345−356.
(65) Treboux, G.; Layrolle, P.; Kanzaki, N.; Onuma, K.; Ito, A. Symmetry of Posner's Cluster. *J. Am. Chem. Soc.* **2000**, *122* (34), 8323−8324.
(66) Posner, A. S.; Betts, F. Synthetic amorphous calcium phosphate and its relation to bone mineral structure. *Acc. Chem. Res.* **1975**, *8* (8), 273−281.

https://doi.org/10.1021/acs.chemmater.3c02346
Chem. Mater. 2023, 35, 10645−10657

(67) Madsen, H. E. L. Solubility Product of Ni-Struvite, $NH_4NiPO_4 \cdot 6H_2O$, at 25°C. *Adv. Chem. Eng. Sci.* **2017**, *07* (02), 206−214.
(68) Rumble, J.; Lide, D.; Bruno, T. *CRC Handbook of Chemistry and Physics*; CRC Press: Cleveland, Ohio, 1977; pp 5−189.
(69) Docherty, R.; Clydesdale, G.; Roberts, K. J.; Bennema, P. Application of Bravais-Friedel-Donnay-Harker, attachment energy and Ising models to predicting and understanding the morphology of molecular crystals. *J. Phys. D: Appl. Phys.* **1991**, *24* (2), 89−99.
(70) Donnay, J. D. H.; Harker, D. A new law of crystal morphology extending the Law of Bravais. *Am. Mineral.* **1937**, *22*, 446−467.
(71) Bach, S.; Panthöfer, M.; Bienert, R.; de Oliveira Guilherme Buzanich, A.; Emmerling, F.; Tremel, W. Role of Water During Crystallization of Amorphous Cobalt Phosphate Nanoparticles. *Cryst. Growth Des.* **2016**, *16* (8), 4232−4239.
(72) De Yoreo, J. Crystal nucleation: more than one pathway. *Nat. Mater.* **2013**, *12* (4), 284−285.
(73) De Yoreo, J. J.; Gilbert, P. U.; Sommerdijk, N. A.; Penn, R. L.; Whitelam, S.; Joester, D.; Zhang, H.; Rimer, J. D.; Navrotsky, A.; Banfield, J. F.; Wallace, A. F.; Michel, F. M.; Meldrum, F. C.; Colfen, H.; Dove, P. M. Crystallization by particle attachment in synthetic, biogenic, and geologic environments. *Science* **2015**, *349* (6247), No. aaa6760.
(74) Rodriguez-Blanco, J. D.; Shaw, S.; Benning, L. G. The kinetics and mechanisms of amorphous calcium carbonate (ACC) crystallization to calcite, viavaterite. *Nanoscale* **2011**, *3* (1), 265−271.
(75) Tobler, D. J.; Rodriguez-Blanco, J. D.; Dideriksen, K.; Bovet, N.; Sand, K. K.; Stipp, S. L. S. Citrate Effects on Amorphous Calcium Carbonate (ACC) Structure, Stability, and Crystallization. *Adv. Funct. Mater.* **2015**, *25* (20), 3081−3090.

https://doi.org/10.1021/acs.chemmater.3c02346
Chem. Mater. 2023, 35, 10645−10657